

Bandstructure Effects in Silicon Nanowire Electron Transport

Neophytos Neophytou, Abhijeet Paul, Mark Lundstrom and Gerhard Klimeck
School of Electrical and Computer Engineering, Purdue University, West Lafayette,
Indiana 47907-1285
Email: neophyto@purdue.edu

ABSTRACT

The effects of bandstructure on the electronic transport of strongly quantized silicon nanowire field effect transistors are examined. The energy dispersion relations are computed using a 10-band $sp^3d^5s^*$ semi-empirical atomistic tight-binding model coupled to a self consistent Poisson solver. A semi-classical, ballistic FET model is then used to evaluate the current-voltage characteristics of nanowires in various transport orientations. The dispersion of nanowires, is generally thought of as a quantity only determined by the material properties and the device geometry. This work reveals that it changes under charge filling of the lattice. For wires with dimensions below 5nm, the effective masses change significantly with quantization, and change differently for different transport orientations. In addition, effects such as valley splitting, lift the degeneracies of the bands in a non-trivial manner. This is particularly evident in the [110] transport direction. Due to the low 1D density of states, at high inversion conditions the dispersion curves can shift by several kT below the Fermi level, which results in a large dependence of the nanowire injection velocity and quantum capacitance on the gate bias. These quantities strongly depend on the dispersion of the wires and reflect on their transport characteristics. The different behavior of the nanowire dispersion under different quantization sizes and transport orientations can be explained from the non-parabolicities and anisotropies that reside in the first Brillouin zone of silicon.

Index terms – nanowire, bandstructure, tight binding, transistors, MOSFETs, non-parabolicity, effective mass, injection velocity, quantum capacitance, anisotropy.

1. Introduction

As transistor sizes shrink down to the nanoscale, CMOS development investigates alternative structures and devices [1]. Existing CMOS field-effect transistors are expected to evolve from planar to 3D non-planar devices at nanometer sizes. A possible device approach that has attracted large attention recently because of its possibility of enhanced electrostatic control, is the use of nanowires transistors as field effect devices. Nanowire transistors of diameters even down to 3nm have already been demonstrated by various experimental groups [2-4]. Such devices will operate under strong confinement and strain, regimes where atomistic effects are important. This work investigates atomistic effects in the transport properties of nanowire devices by using a nearest-neighbor tight binding model ($sp^3d^5s^*$) [5-7] for electronic structure calculation, coupled to a 2D Poisson solver for electrostatics. The ballistic transport characteristics are calculated with a semi-classical ballistic model [8,9] (Fig. 1a). Square nanowires of 3nm width, oriented in [100], [110] and [111] transport directions are considered (Fig. 1b), however the main conclusions of this work will be valid for other nanowire cross sections (i.e. cylindrical) since the electronic properties of nanowires are a much more sensitive function of the quantization size rather than the quantization shape [10]. The oxide thickness is assumed to be 1.1nm thick SiO_2 .

The dispersion of small size nanowires is usually considered to be a material parameter, and under strong confinement a property of the geometry, but independent of charge filling of the lattice. It is shown here, however, that even at small scales such as down to 3nm sizes, the wires' dispersion relation changes under charge filling of the lattice, and degeneracies can also be lifted [11,12]. The effect of potential variations in the cross section of the nanowire will also reflect on the shape of the wavefunction, which determines the location of the charge distribution in the channel. In these simulations, even under high inversion conditions, the wavefunction is pushed almost half a nanometer away from the Si/ SiO_2 interface. This well known shift of the wavefunction away from the interface, together with the low one-dimensional (1D) density of states of the nanowire, effectively increases the oxide thickness by 0.54nm and therefore reduces the total capacitance of the transistor by 30%. The small 1D density of

states allows for the Fermi level to be pushed deeply into the conduction band for the adequate amount of charge to be accumulated into the channel. As the slope of the dispersion increases at higher energies, the injection velocity also significantly increases for nanowires in all transport orientations (19% in the [110] and up to 30% in the [100] and [111] wire orientations).

In addition to the effect of potential variations, the wire dimension and orientations have a strong influence on both, quantization and transport masses that undergo large changes as the wire dimension shrinks [10], as well as on the valley splitting in the dispersion of the nanowires. This paper, shows how this behavior results from the non-parabolicity and anisotropy of the Si bandstructure that is particularly evident in strongly quantized nanowires and directly reflects on their transport properties. The tight-binding model used in this work, can successfully reproduce experimental evidence for the measurement of the bandgap of [112] nanowires [13-15]. Since the bandgap of quantized systems is a strong function of the quantization masses in the two transverse directions, a verification of the experimentally deduced bandgap supports the theoretical prediction for the behavior of the wires' masses under strong quantization. Wires in [110] transport orientation experience a reduction in the electron transport effective mass compared to [100] or [111] oriented wires.

Due to this variation in the masses, the degeneracies of the valleys, and the position of heavier upper valleys in energy, the quantum capacitance (C_Q) is a complicated function of the gate bias and different for wires in different orientations. It is shown, however, that although its' small value adds to the degradation of the total gate capacitance, its' effect is not prominent in the transport properties of one wire orientation over another. The total gate capacitance is almost equivalent in all wire orientations. In terms of on-current capabilities therefore, transport at small nanowire dimensions will be preferable in the [110] oriented devices that has the lowest mass and highest carrier velocities, closely followed by the [100] devices with a little higher masses, but twice the degeneracies of the lowest subbands. The same results can be obtained from a full 3D quantum (NEGF) simulations [16], but the simple model used here provides physical insight.

Therefore, four significant components of how bandstructure affects the device transport characteristics are identified. First, is the change of the dispersion with charge filling of the lattice and the well-known shift the wavefunction away from the Si/SiO₂ interface. This, together with the low 1D density of states, results in large degradation of the total gate capacitance. Second, is the large increase in injection velocity as the gate bias increases, with the [110] wires to have the fastest carriers. Third, is the valley splitting at small diameters which appears to be particularly evident again in the [110] wire orientation. Forth, is the significant change in the effective mass of the nanowires under spatial confinement. All these components appear of course in UTB devices and nanoscale MOSFETs, however, they are significantly more enhanced in the case of nanowires [17,18].

2. Approach

The model device simulated is a rectangular nanowire of 3nm x 3nm dimensions in various transport orientations. Unless otherwise stated, the specified wire orientation is always the transport one. Three different orientations are investigated in this work, [100], [110] and [111]. The atomic arrangement in each case is different as shown in Fig. 1b. The simulation procedure consists of three steps as shown in Fig. 1a and described below:

1. First, the bandstructure of the wire is calculated using an atomistic tight-binding model. In this case, each atomic site in the zincblende lattice is represented by a $sp^3d^5s^*$ basis in the wire Hamiltonian. Since only the conduction band is treated in this paper, the spin-orbit coupling is ignored. This approximation favors computational efficiency, without affecting the accuracy of the results. The atoms that reside on the surface of the nanowire are hydrogen passivated in the sp^3 hybridization scheme [19]. This technique successfully removes all dangling bonds which otherwise will accumulate in the bandgap energy region of the device. Any effect of surface reconstruction or surface imperfections is not considered in this study.

2. The charge is computed using the calculated bandstructure and a simple semiclassical ballistic model [8,9]. In this model the positive going states in the dispersion of the nanowire are filled by the source Fermi level, and the negative going states are filled by the drain Fermi level.
3. In step three, using this charge distribution (after it is collapsed on the 2D cross sectional plane of the wire) a 2D Poisson is solved to obtain the electrostatic potential in the device. The wavefunction of each state determines the distribution of its charge in each of the orbital sites of the system (and therefore the spatial distribution of charge). The potential is then included into the Hamiltonian (step 1) for a new calculation of the bandstructure, until self consistency is achieved.

To investigate the bandstructure effects under different quantization sizes, the equilibrium dispersion (flat potential in the Hamiltonian) is calculated for different wire sizes and orientations. The effect of valley splitting is computed, as well as the masses of the Γ and X valleys. It is found that wires oriented along [110] have a decrease in their transport masses, whereas wires in [100] and [111] directions have a large increase. In order to investigate the origin of this different behavior, slices of the 3D bulk bandstructure of the 1st Brillouin zone (*BZ*) are taken at the X point. Although in bulk MOSFETs a small part of the *BZ* near the *Ec* minimum is participating in transport, the important part of the *BZ* under strong quantization is actually shifted in different points in the *BZ*, in which the curvatures (that define the masses) can be significantly different.

3. Results and Discussion

Figure 2 shows device features for a 3nm square [100] oriented nanowire under low and high gate biases. (In this work the drain bias used is $V_D=0.5V$ in all cases). Under low gate biases, the lattice is almost empty of charge (Fig. 2a) and the dispersion relation (Fig. 2c) is the equilibrium dispersion. Under high biases, there is significant charge filling of the lattice (Fig. 2b). The charge distribution takes the shape of the underlying atomic positions. This causes changes in the dispersion of the nanowire as shown in Fig.

2d. Here, the excited states at Γ shift down, and reside now below the X point valleys [20]. The charge here cannot pile up at the interface, but resides almost 0.5nm away from the interface, causing an increase in the effective oxide thickness of the nanowire.

Different wire orientations have different dispersion relations, but react similarly under potential variations in the lattice. The position of the bands shifts and degeneracies can also be lifted. Figure 3a-b shows the $E(k)$ of a [110] oriented nanowire under low and high biases. Noticeable here is the larger variation in the dispersion under charge filling of the lattice. The band degeneracies are lifted (from 2 to 1) by several meV. Fig. 3c-d shows the same features for a [111] oriented wire. This wires' $E(k)$ is less sensitive to lattice charge filling. The degeneracy of the bands of this wire is 3 because of the symmetry between the transport axis (or equivalently the quantization plane in the perpendicular direction) and the three pairs of ellipsoids in the Si bandstructure. Under high biases, there exists some left of degeneracies, but not enough to influence the transport properties. Figure 3e-f shows the charge and injection velocity of the three different oriented wires as a function of the distance of the Fermi level from the conduction band edge. Quantities for two cases are calculated: (a) The Fermi level "scans" the equilibrium bandstructure and the charge and injection velocities are extracted, and (b) the results are extracted from the self-consistent calculations with potential variations in the lattice taken into consideration. There is no significant difference in these extracted quantities due to the potential variations, and the self-consistent vs. non-self-consistent curves fall almost on top of each other. However, the self consistently extracted bandstructure corresponds to a different wavefunction shape which reflects to a different charge distribution in space. This is the quantity that causes degradation of the total gate capacitance as will be shown later and affects the transport, and not the dispersion changes by themselves. (In an earlier work, [20], it is shown that the current-voltage characteristics can significantly vary if the spatial variation of the charge is not considered). For this example however, a large drain bias ($V_D=0.5V$) is used. Under low drain biases ($V_D=1meV$) however, evidence of the bandstructure differences in these two quantities as well as other quantities such as the transconductance are more possible to appear. The charge in Fig. 3e for a certain position of the Fermi level is always higher in the [111] due the higher density of states and valley

degeneracy. The reverse trend is observed in Fig. 3f, where [110] wire has the highest velocity at due to its' lighter mass. Noticeable here, is the fact that the carrier velocity in the [100] wire approaches the [110] velocity as the Fermi level is pushed into the conduction band. As higher k-states are occupied, the velocity increases since it is proportional to the slope of the bands. In the [110] case however, the heavier upper valleys appear a few meV earlier than in the [100] case, which slows carriers down. Also, non-parabolicity is more enhanced in the [110] case in higher energies rather than in [100] wires, which does not let the carries increase their speed as fast.

Figure 4a shows a performance comparison between the wires in different orientations, [100], [110] and [111]. To investigate that, in Fig. 4a the total gate capacitance (C_G) vs. gate bias (V_G) of the three wires is shown at the same I_{OFF} . The total capacitance in the three wires is very similar for all gate biases, which indicates that the total charge in the devices is also very similar. (The [111] wires' charge is slightly higher due to the small enhancement of its' capacitance over the other wires). The capacitance value is degraded from the oxide capacitance by an amount that corresponds to an effective increase in the oxide thickness. The effective increase in the oxide thickness in these cases is calculated to be 0.54nm, which is 50% of the physical gate oxide thickness ($t_{ox}=1.1nm$). Using the values of the oxide capacitance and the total gate capacitance at high V_G , the value of the semiconductor capacitance (C_S) can be computed. This number

can be extracted from $C_G = \frac{C_S C_{ox}}{C_S + C_{ox}}$ (the total capacitance is the series combination of

the semiconductor and the oxide capacitance). The oxide capacitance of this rectangular structure is 0.483 nF/m and is calculated numerically using a 2D Poisson solver that takes the fringing at the edges into consideration. From this relation, C_S can be computed to be $C_S = 0.8nF / m$, only twice the value of the oxide capacitance. The first reason for this large degradation is the shift of the wavefunction away from the oxide/semiconductor interface inside the channel by almost 0.5nm as shown in Fig. 2b. The second reason, is the small value of the quantum capacitance (C_Q). The C_Q for all three devices vs. V_G is shown in Fig. 4b. This quantity is a measure of the density of states at the Fermi level. In all wire cases, C_Q is not a constant value, but undergoes large transitions as the Fermi level is pushed inside the conduction band (E_c) at large gate biases. The [111] wire has

the largest C_Q at most bias range because of the higher mass ($m^*=0.46m_0$, where m_0 is the free electron mass) and higher degeneracy of its' valleys ($D=6$). At high biases, the upper valleys of the [100] and [110] wires start to be populated, whereas the [111] wire starts to lose half of its bands due to strong interactions with higher valleys in its' bandstructure as shown in Fig. 3. As a result, the C_Q of [111] the wire drops below the [100] and [110] wires' values. On the other hand, at low biases, the [110] wire has the lowest quantum capacitance because of the lower mass ($m^*=0.16m_0$) and lower degeneracy of its' valleys ($D=2$). Because of its' low degeneracy, however, the Fermi level can be pushed further into the conduction band and occupy the upper valleys faster. Once this happens, C_Q for the [110] wire overpasses the C_Q for the [100] wire. (The [100] wire, has mass $0.27m_0$ and degeneracy of four ($D=4$)). The exact reasons why the masses have these values will be addressed later on in the paper. These differences, however, are not that great to influence the transport properties of the devices at large. As computed earlier, the semiconductor capacitance, C_S , which takes into account both the charge distribution, as well as the C_Q , is degraded from the C_Q value. The values of C_Q for the high V_G cases are around 3nF/m , numbers larger than the C_S value. (Similar deviations of the semiconductor capacitance from the quantum capacitance have also been observed in thin body devices [21]). This shows that the C_Q is only partially responsible for the total capacitance degradation, with a large part of the degradation coming from the wavefunction shape itself. The variations in the C_Q values of the different wires are therefore smeared out, and the C_G is almost the same for all three wires. (This observation can of course be different in the case of high-k dielectric oxides, in which the importance of C_Q can be more pronounced).

Figure 4c shows the injection velocities of the wires vs. gate bias (V_G). The [110] wire has the largest velocities whereas the [111] wire has the lowest velocities. In all cases, the injection velocities are not constant, but increase as the lattice is filled with charge because faster high energy carrier states are being populated. This increase can reach even up to 30% in the [100] and [111] wire cases. At low biases, the masses of the lowest valleys will determine the velocities of the carriers. (In 1D the velocity is proportional to $1/\sqrt{m^*}$). As a result, the [110] wire with $m^*=0.16m_0$ will have the higher velocity, followed by the [100] wire with mass $m^*=0.27m_0$, and finally by the [111] wire

of mass $m^*=0.53m_0$. As indicated above, the total charge in the three wires is almost the same. In such a case, the Fermi level will be pushed in the conduction band until the charge from the occupied states satisfies charge neutrality with the gate charge. The larger density of states of the [111] wire and its' larger degeneracy do not allow the Fermi level to be pushed far into the conduction band. Therefore, only the lower energy and slower carries are used, and the velocity in this case is low. In the [110] wire case, the degeneracy is 2, and the subband density of states low, therefore the Fermi level will be pushed far into the conduction band, and faster carries will be utilized as shown in Fig. 4c. The velocity difference directly reflects on the I_{DS} as shown in Fig. 4d in which the drive current capabilities of the wires are compared at the same off-current (I_{OFF}). The [110] and [100] wires perform better than the [111] wire in terms of on-current capabilities. Notice here is that the bandstructure of the wires is a very sensitive function of its quantization, and these specific results presented here can be different for different wire sizes or biases. The [110] wire stands 5% higher than the [100] wire, because of its' lower mass. The [100] wire, however, has a larger degeneracy at Γ , so the heavier upper valleys are hard to be reached. These two factors, masses and degeneracies determine which device will perform best, and their order can change depending on quantization or even gate biases.

The effect of valley splitting, in which the degeneracies of the bands are lifted [10,12,17], is particularly evident in the [110] wires not only under electrostatic, but also spatial quantization. Figure 5a-b shows the $E(k)$ of a 2nm wire in the [100] and [111] orientations. A slight valley splitting of the degenerate valleys under quantization is observed. In the case of the [100] the splitting is 10meV and in the case of the [111] wire, 24meV. These are values lower or close to $kT=26meV$ and are not expected to have a significant effect in the transport properties of the nanowires. In the case of the [110] wire however, the valleys splitting is larger. Figure 5c shows the $E(k)$ of a 2nm [110] wire. Both Γ and off- Γ valleys experience valley splitting of their degenerate valleys of 76meV and 14meV respectively. Figure 5d shows how this effect varies with the spatial confinement in the [110] wire. Although large nanowires ($>5nm$) are not affected, the valleys splitting can reach up to 200meV for the Γ valleys of narrow wires with sizes below 2nm. The valley splitting of the off- Γ valleys however, is not affected as much.

Only a few tenths of meVs of splitting are observed in this case. (It is noted here that the splitting in the other wire orientations is smaller than the [110] wires of similar quantization sizes even for wires below 2nm).

The transport mass of the wires is also a quantity affected by quantization, and together with the degeneracy of the wires is probably the most important quantity that affects the transport properties. The injection velocity and quantum capacitance strongly depend on the masses. Both the quantization and the transport masses of nanowires under arbitrary wire orientations are certain combinations of the longitudinal ($m_l=0.89m_0$) and the transverse effective masses ($m_t=0.19m_0$) of the Si ellipsoids. Figure 6a shows the three pairs of ellipsoids that form the conduction band minima in Si, each characterized by the x,y and z directional masses. The masses of the valleys that appear in the nanowire dispersion are automatically accounted in tight-binding. Of course under quantization, the exact values of these masses are changed from their bulk values. It is mentioned above that the mass at the Γ -point of the [100] and [110] wires are $0.27m_0$ and $0.16m_0$ respectively. These values differ from the expected value, which is the bulk mass value of $0.19m_0$. Figure 6b shows the variation in the lowest valley transport masses as the dimension of the wires' cross section reduces. At large wire cross sections, the [100] and [110] that are located at Γ , approach the bulk transverse mass $m_t=0.19m_0$. The mass of the [111] wire is larger since it is a combination of $m_t=0.19m_0$ and $m_l=0.89m_0$ (the bulk value is $0.43m_0$). As the wire dimensions shrink, the masses increase in the cases of the [100] and [111] oriented wires, but reduce for [110] wires. The off- Γ valley masses of [100] and [110] wires also increase as the dimensions reduce (Fig. 6c). In both cases, the bulk masses in all orientations are noted for reference [22,23]. Notice that in the case of [100] and [110] wires the conduction band minima is located at the Γ point since the quantized Δ valleys project there. In the [111] case however, the conduction band minimum is located at 0.37 of the Brillouin zone (normalized to 1) as seen in Fig.3c,d. (The length of the unit cell in [111] is $L_{111} = \sqrt{3}a_0$. Therefore, the Brillouin zone of a 1D nanowire in [111] extends from $-\frac{\pi}{\sqrt{3}a_0}$ to $\frac{\pi}{\sqrt{3}a_0}$. The Δ valleys in bulk Si are located at $k_x = 0.815 \cdot 2\pi / a_0$. Under quantization in (111) surface they project on the [111] axis at

$k_{[111]} = 0.815 \cdot 2\pi / (\sqrt{3}a_0) = 1.63\pi / (\sqrt{3}a_0)$. The valley projection point falls in the 2nd Brillouin zone. It is then folded in the first Brillouin zone by $k_{[111]} = 1.63\pi / (\sqrt{3}a_0) - 2\pi / (\sqrt{3}a_0) = 0.37\pi / (\sqrt{3}a_0)$. After normalization to the length of the Brillouin zone, the valleys appear at $k_{[111]} = 0.37$.

This distinctly different observation in the masses of wires is a result of the non-parabolicity and anisotropy of the Si bandstructure. Under any quantization, the subband levels will follow the “particle in a box” quantization, as shown in Fig. 7(a). The stronger the quantization, the higher the energy levels of the subbands. In the case of Si, to estimate the quantization levels of the conduction band ellipsoid quantized along the longitudinal direction, the energy contour in the x - y plane near the band minima is plotted as shown in Fig. 7(b). (“Cut” through the ellipsoid along its’ longitudinal axis). Similarly to Fig. 7(a), quantization of 2nm, 3nm, and 5nm will shift the energy levels to the lines shown in the figure. The energy levels at these lines will be the relevant subbands in a thin body quantization (single axis of quantization). Figure 7(c) now, shows the energy contour taken at the 3nm line, perpendicular to the contour of Fig. 7(b). An extra quantization in the z -direction (as in the wire case) means that the relevant 1D bands are the ones located at the horizontal lines of Fig. 7(c). These subbands are plotted in Fig. 7(d) for the cases of 2nm, 3nm and 5nm. (The x -direction quantization is 3nm in all cases). The mass of these bands is the transport mass (y -direction) that the wire has in the [010] orientation, which tends to increase with stronger quantization. Similarly the transport masses of wires in other orientations can be explained. Evident in the bandstructure is the anisotropy which results in different behavior in the quantization of the [100] to quantization of the [110] axes. For example, quantization of the [110] axis (equivalently [110] transport direction), results in reduction of the transport masses. (Similar anisotropic results have been also obtained using empirical non-local pseudopotential and ab-initio GW calculations [24]).

4. Conclusions

Transport properties of nanowires in different transport orientations ([100], [110] and [111]) were examined using a 10 orbital $sp^3d^5s^*$ atomistic TB model self consistently coupled to a 2D Poisson solver. A semiclassical ballistic model was used to calculate the current-voltage characteristics of the nanowires. It is found that the dispersions of the nanowires undergo changes under gate bias, which at some cases can cause large lift of degeneracies. The quantum capacitance of the different oriented 3nm wires that were investigated is a strong function of gate bias, but of similar order in all wires. Together with the spatial variation of the wavefunction in the cross section of the device, it causes degradation to the total gate capacitance. The total gate capacitance of all nanowire devices investigated is almost the same, however, indicating that the charge in the devices is also of similar order. [110] oriented wires have the maximum injection velocities due to their light effective mass, whereas [111] oriented wires the lowest injection velocities due to their higher masses. At higher biases, the velocities of the [100] wire carries approaches the [110] velocities. The injection velocities reflect directly on the current capabilities of the wires, with the [110] and [100] oriented wires to indicate the best performance in terms of on-current capabilities compared to the [111] wires which are the worse. The masses of the wires and effects such as valley splitting are a sensitive function of the wire dimensions (below 7nm), and reflect on the output performance of nanowire devices. This is an effect that resides in the anisotropy of the Si Brillouin zone that is particularly important in strongly quantized devices. Finally, the authors would like to mention that the simulator used in this study will be released as an enhanced version of the Bandstructure Lab on nanoHUB.org [25]

5. Acknowledgements

This work was funded by the Semiconductor Research Corporation (SRC) and MARCO MSD Focus Center on Materials, Structures and Devices. The computational

resources for this work were provided through nanoHUB.org by the Network for Computational Nanotechnology (NCN). The authors would like to acknowledge Prof. Mark Schilfgaarde of Arizona State University for ab-initio GW calculations and Dr. Tony Low of Purdue University for pseudopotential calculations for benchmarking of bandstructure results.

References

- [1] ITRS Public Home Page. <http://www.itrs.net/reports.html>
- [2] N. Singh et. al., “Ultra-narrow silicon nanowire gate-all-around CMOS devices: Impact of diameter, channel-orientation and low temperature on device performance,” *Int. Elec. Dev. Meeting*, 2006.
- [3] K. H. Cho, “Observation of single electron tunneling and ballistic transport in twin silicon nanowire MOSFETs (TSNWFETs) fabricated by top-down CMOS process,” *Int. Elec. Dev. Meeting*, 2006.
- [4] J. Xiang, W. Lu, Y. Hu, Y. Wu, H. Yan, and Charles M. Lieber, “Ge/Si nanowire heterostructures as high-performance field-effect transistors,” *Nature*, vol. 441, no. 25, 2006.
- [5] G. Klimeck, F. Oyafuso, T. B. Boykin, R. C. Bowen, and P. von Allmen, *Computer Modeling in Engineering and Science (CMES)*, vol. 3, no. 5, pp. 601-642, 2002.
- [6] T. B. Boykin, G. Klimeck, and F. Oyafuso, “Valence band effective-mass expressions in the $sp^3d^5s^*$ empirical tight-binding model applied to a Si and Ge parametrization,” *Phys. Rev. B*, vol. 69, pp. 115201-115210, 2004.
- [7] G. Klimeck, S. Ahmed, H. Bae, N. Kharche, S. Clark, B. Haley, S. Lee, M. Naumov, H. Ryu, F. Saied, M. Prada, M. Korkusinski, and T. B. Boykin, “Atomistic simulation of realistically sized nanodevices using NEMO 3-D—Part I: Models and benchmarks,” *IEEE Transactions on Electron Devices*, vol. 54, no. 9, pp. 2079-2089, 2007.
- [8] M.S. Lundstrom, and J. Guo, “Nanoscale transistors: Device physics, modeling and simulation,” *Springer*, 2006.

- [9] A. Rahman, J. Guo, S. Datta, and M. Lundstrom, "Theory of ballistic nanotransistors," *IEEE Transactions on Electron Devices*, vol. 50, no. 9, pp. 1853-1864, 2003.
- [10] J. Wang, A. Rahman, A. Ghosh, G. Klimeck, and M. Lundstrom, "On the validity of the parabolic effective-mass approximation for the I-V calculation of silicon nanowire transistors," *IEEE Transactions on Electron Devices*, vol. 52, no. 7, pp. 1589-1595, 2005.
- [11] T. B. Boykin, G. Klimeck, M. Friesen, S. N. Coppersmith, P. von Allen, F. Oyafuso, and S. Lee, "Valley splitting in strained silicon quantum wells," *Appl. Phys. Lett.*, vol. 84, no. 1, pp.115, 2004.
- [12] T. B. Boykin, G. Klimeck, M. Friesen, S. N. Coppersmith, P. von Allen, F. Oyafuso, and S. Lee, "Valley splitting in low-density quantum confined heterostructures studied using tight-binding models," *Phys. Rev. B*, vol. 70, pp.165325, 2004.
- [13] D.D.D. Ma et.al., "Small-diameter silicon nanowire surfaces," *Science*, 299, 1874, 2003.
- [14] J. Wang, PhD thesis, Purdue University, 2005.
- [15] X. Zhao, C. M. Wei, L. Yang, and M. Y. Chou, "Quantum confinement and electronic properties of silicon nanowires," *Phys. Rev. Lett.*, vol. 92, no. 23, pp. 236805, 2004.
- [16] M. Luisier, A. Schenk, W. Fichtner, "Full-Band Atomistic Study of Source-To-Drain Tunneling in Si Nanowire Transistors," Proc. of SISPAD, 978-3-211-72860-4, pp. 221-224, 2007.

- [17] A. Rahman, G. Klimeck, M. Lundstrom, T. B. Boykin, and N. Vagidov, "Atomistic approach for nanoscale devices at the scaling limit and beyond – Valley splitting in Si," *J. J. Appl. Phys.*, vol. 44, no. 4B, pp. 2187-2190, 2005.
- [18] Y. Liu, N. Neophytou, T. Low, G. Klimeck, and M. Lundstrom, "A tight-binding study of the ballistic injection velocity for ultra-thin-body SOI MOSFETs," *IEEE Transactions on Electron Devices*, submitted.
- [19] S. Lee, F. Oyafuso, P. Von, Allmen, and G. Klimeck, "Boundary conditions for the electronic structure of finite-extent embedded semiconductor nanostructures," *Phys. Rev. B*, vol. 69, pp. 045316-045323, 2004.
- [20] N. Neophytou, A. Paul, M. Lundstrom and G. Klimeck, "Self-consistent simulations of nanowire transistors using atomistic basis sets," *SISPAD 2007*, to appear.
- [21] H. S. Pal, K. D. Cantley, Y. Liu & M. S. Lundstrom, "Semiconductor capacitance and injection velocity considerations for bulk and SOI MOSFETs with alternate channel materials," submitted to *IEEE TED*.
- [22] M. Bescond, N. Cavassilas, and M. Lannoo, "Effective-mass approach for n-type semiconductor nanowire MOSFETs arbitrarily oriented," *Nanotechnology*, vol. 18, pp. 255201, 2007.
- [23] A. Rahman, M. S. Lundstrom, and A. W. Ghosh, "Generalized effective-mass approach for n-type metal-oxide-semiconductor field-effect transistors on arbitrarily orientated wafers," *J. Appl. Phys.*, vol. 97, pp. 053702-053713, 2005.
- [24] Personal communication with Prof. Mark Schilfgaarde (Arizona State University) for the GW calculations and with Dr. Tony Low (Purdue University) for the pseudopotential calculations. A comparison between the methods will be published in the future.

[25] [nanoHub] Bandstructure lab on nanoHUB.org
(<https://www.nanohub.org/tools/bandstrlab/>)

Figure Captions

Figure 1:

(a) Schematic of the simulation procedure. Using an atomistic $sp^3d^5s^*$ -SO tight-binding model, the bandstructure of the nanowire under consideration is calculated. A semiclassical ballistic model is then used to calculate the charge distribution in the wire from the source and drain Fermi levels. The charge is used in a 2D Poisson for the electrostatic solution of the potential in the cross section of the wire. The whole process is done self consistently. (b) The lattice in the transport wire orientations used – [100], [110] and [111].

Figure 2:

Device features for a 3nm [100] rectangular wire. (a-b) The 2D cross section showing the charge distribution under low and high gate biases, respectively. Even under high bias, the charge distribution is located almost half a nanometer away from the oxide. This causes degradation in the total capacitance of the wire. The dots indicate the underlying atomic positions. (c-d) $E(k)$ plots for the cases (a-b). The bandstructure features change under self consistency. E_{fs} is the source Fermi level. (Zero energy indicates the conduction band edge.)

Figure 3:

(a-b) The bandstructure of a 3nm [110] oriented nanowire under low bias (a) and high bias (b). Under high biases the degeneracies of the Γ valley are lifted from 2 to 1. (c-d) The bandstructure of a 3nm [111] oriented nanowire under low bias (c) and high bias (d). (e) The charge distribution as a function of the difference of the conduction band edge from the Fermi level for two cases: (1) The Fermi level “scans” the equilibrium bandstructure and the charge is extracted, and (2) the charge is extracted from the self-consistent calculations with potential variations in the lattice taken into consideration. (f) The injection velocity for the same case as (e). The changes in the dispersion themselves do not reflect much on the charge distribution or the injection velocities. The differences

between the two models result from the spatial information of the wavefunction that corresponds to the bandstructure changes.

Figure 4:

(a) The gate capacitance C_G vs. gate bias (V_G) for wires in [100], [110] and [111] directions. The capacitance is degraded from the oxide capacitance by an amount that corresponds to an increase in the effective oxide thickness of 0.54nm, but is similar for all wires. (b) The quantum capacitance C_Q vs. V_G of the three devices which is a measure of the density of states at the Fermi level. (c) Comparison between the injection velocities of 3nm nanowires under different orientations vs. V_G . In all cases, the velocity is not constant, but increases as the lattice is filled with charge. (d) The I_{DS} vs. V_G for the three wires at the same I_{OFF} . The velocity difference directly reflects on the currents.

Figure 5:

The effect of valley splitting in small nanowires. (a-c) The $E(k)$ of a 2nm wire in the [100], [111] and [110] orientations respectively. (d) The effect of valley splitting in the [110] wire as the dimensions decrease. The Γ valleys are severely affected at cross sections below 3nm, whereas the off- Γ valleys are not affected as much.

Figure 6:

(a) The three equivalent pairs of ellipsoids in the conduction band of Si are described by the longitudinal and transverse masses. A combination of these masses results in the quantization and transport masses of nanowires under arbitrary orientations. (b) The transport masses oriented in [100], [110] and [111] vs. wire dimension as calculated from TB. At large wire cross sections, the [100] and [110] that are located at Γ , approach the bulk $m_t=0.19m_0$. The mass of the [111] wire is larger since it is a combination of m_t and $m_l=0.89m_0$. As the wire dimensions shrink, the mass of the [110] wire reduces, whereas the masses of the other two wires increase. (c) The off- Γ valley masses for the cases of the [110] and [100] wires. Both increase as the dimensions decrease. (The expected bulk mass values for every orientation are denoted.)

Figure 7:

(a) The energy levels of a quantized structure using the “particle in a box” picture. Under quantization, the subband edges can be deduced from the bulk materials’ dispersion. (b) Energy contour at the middle of one of the Si Brillouin zone ellipsoids calculated using the full 3D k-space information of the Si Brillouin zone. A “cut” through the Si ellipsoid along its’ longitudinal axis is shown. Under quantization in 2nm, 3nm and 5nm, the relevant subband energies are indicated by the vertical lines. (c) A “cut” through the Si ellipsoid perpendicular to its’ longitudinal axis at the 3nm quantization line of (b). The non-parabolicity and anisotropy is evident in this figure. The horizontal lines indicate the relevant energy regions under another quantization in the y-direction for 2nm, 3nm and 5nm quantized structures. (d) The dispersions of the vertical lines in (c). The masses and the band edge of the dispersions will be the ones that appear in a quantized wire. The anisotropy is directly reflected on the masses in the different wire orientations (as in Fig. 6b).

Figure 1

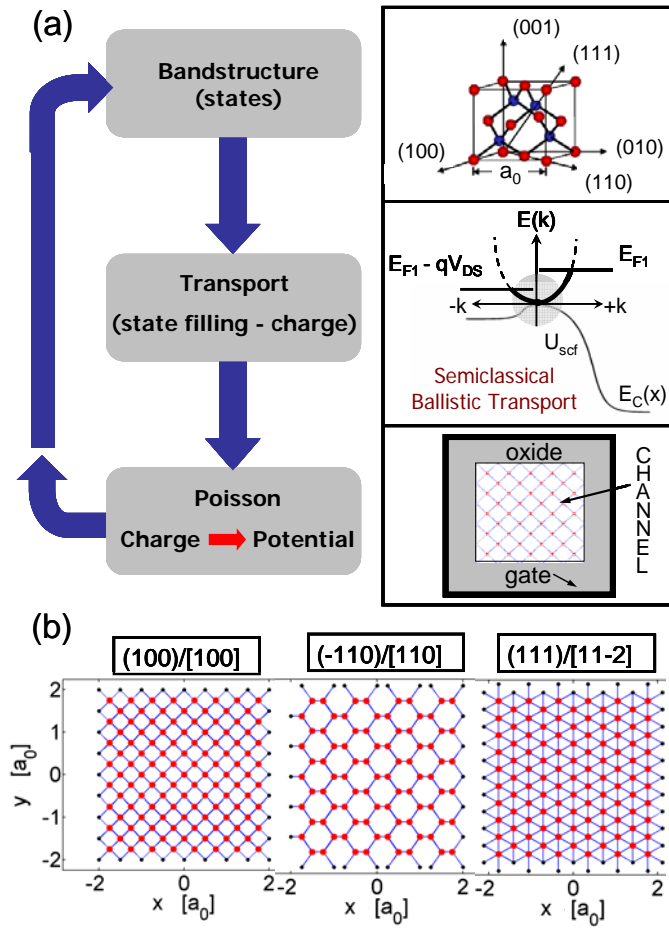


Figure 2

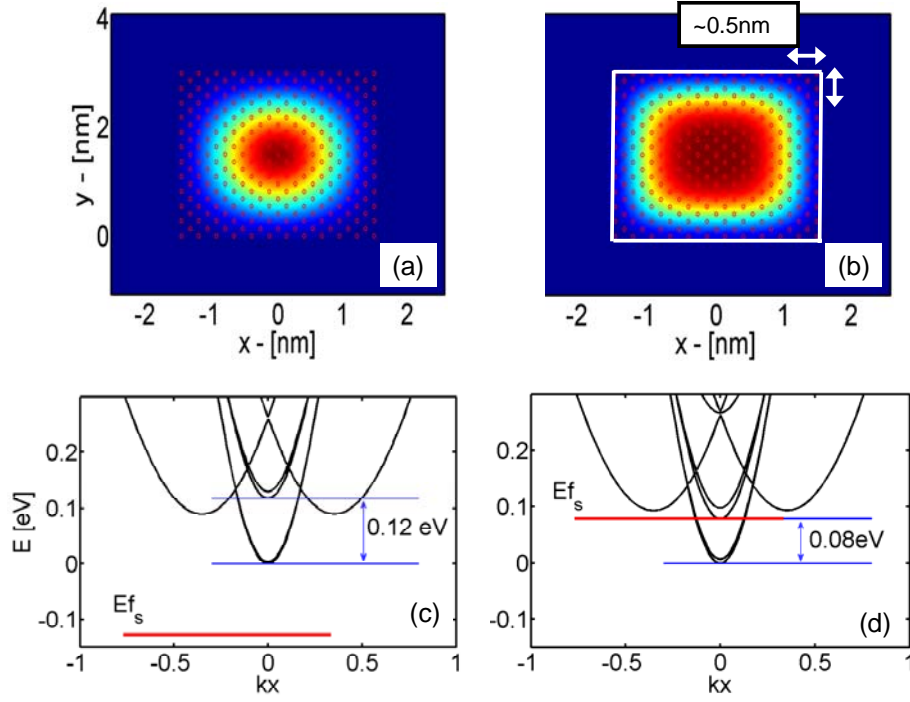


Figure 3

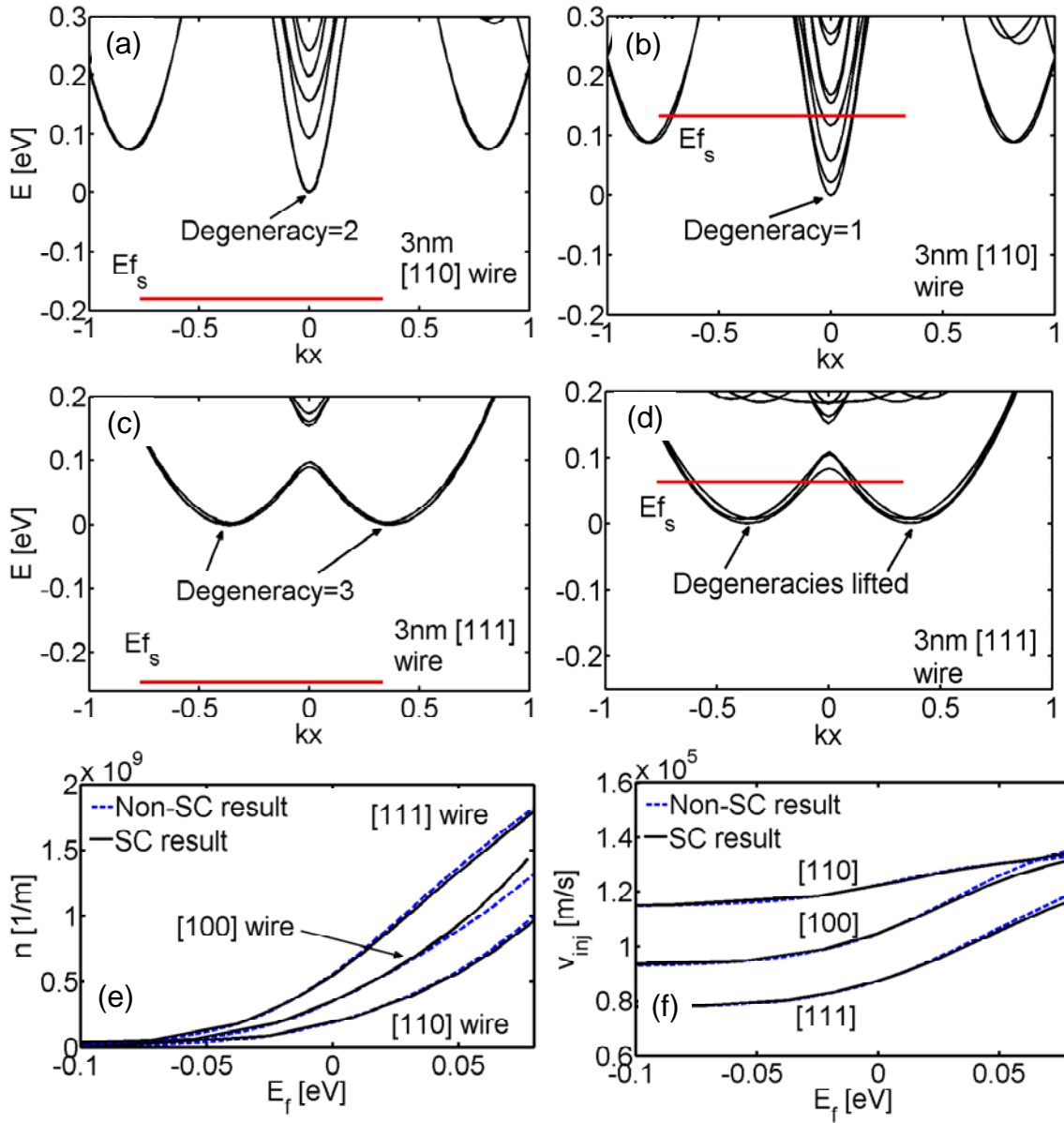


Figure 4

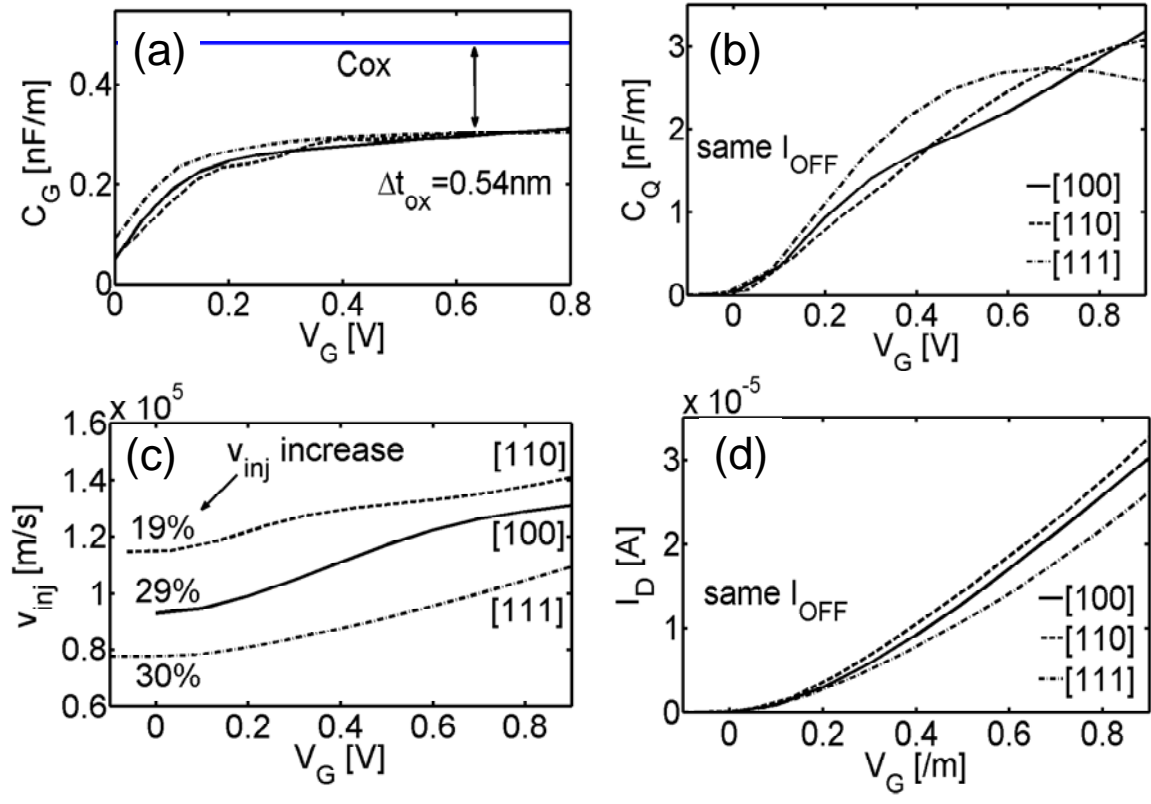


Figure 5

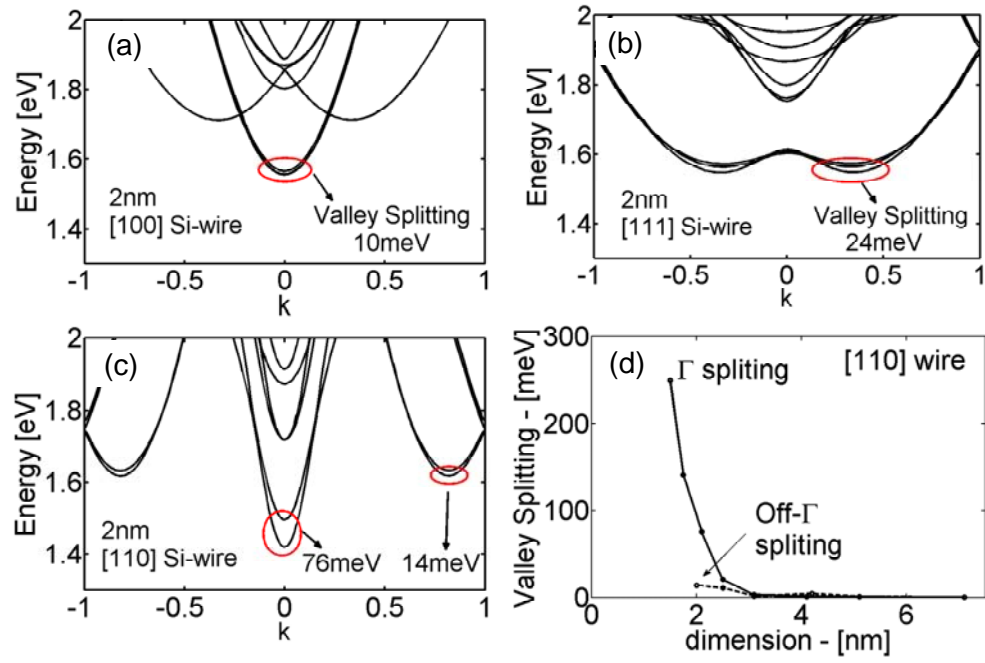


Figure 6

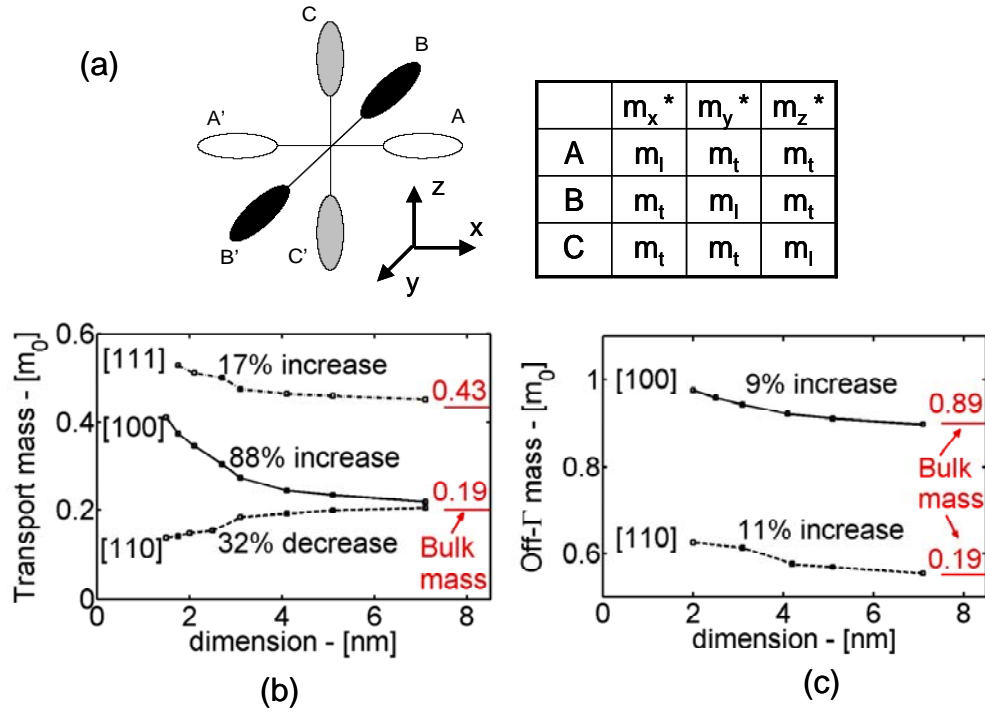


Figure 7

